

Multiphoton amplification processes and quantum-path interferences in a coherently driven atomic vapor

J. J. Fernández-Soler,¹ J. L. Font,¹ R. Vilaseca,¹ Daniel J. Gauthier,² and A. Kul'minskii²

¹*Departament de Física i Enginyeria Nuclear, Universitat Politècnica de Catalunya, Colom 11, E-08222 Terrassa, Spain*

²*Department of Physics, Duke University, Box 90305, Durham, North Carolina 27708, USA*

(Received 2 July 2003; published 24 October 2003)

We develop a theoretical model of two-photon amplification in laser-driven potassium atoms and use it to analyze the recent experiments reported by Pfister *et al.* [Phys. Rev. A **60**, R4249 (1999)]. The model takes into account most of the essential factors influencing the amplification process, including the atomic hyperfine structure (which makes multiphoton emission possible) and the simultaneous interaction with intense drive and probe beams with arbitrary detunings. We determine the origin and analyze the properties of different multiphoton gain resonances that appear in the light-matter interaction. In particular, the influence of the drive and probe field amplitudes and detunings on the strength and frequency of the two-photon amplification resonance is studied in detail, showing clearly the differences with respect to the behavior of single-photon or other multiphoton amplification processes. In addition, we investigate interferences between different quantum pathways originating from the hyperfine structure and determine the conditions under which they can enhance or suppress multiphoton resonances. The predictions of the model are in good agreement with the observations, indicating that it can be used to understand recent experiments on two-photon lasing reported by Pfister *et al.* [Phys. Rev. Lett. **86**, 4512 (2001)].

DOI: 10.1103/PhysRevA.68.043824

PACS number(s): 42.50.Gy

I. INTRODUCTION

Although most amplification and lasing systems are based on single-photon processes, there has always been an interest in the physics of multiphoton processes, such as two-photon amplifiers and lasers [1]. These devices are of interest because their intrinsic nonlinearity can lead to dynamical behaviors such as fast amplifiers, self-pulsing [2], cavity solitons [3], and different quantum states of light [4–6], such as multiphoton entanglement [7].

Theoretical analyses of two-photon amplification and lasing were initiated long ago [8–11], but the difficulties in their experimental realization [12,13] has slowed progress in the field. The main practical difficulty lies in the fact that two-photon amplification processes are often overcome by competing single-photon amplification or multiwave mixing processes [14,15].

Recent experimental achievements, however, are opening the way for the implementation and investigation of the properties of two-photon amplification and laser systems. The initial results by Mossberg and collaborators using barium in 1992 [13] have been followed by more detailed results from Gauthier and collaborators on amplification (1999) [16] and lasing (2001) [7] in potassium using a different atom-field interaction scheme. In these atomic systems, the necessary two-photon population inversion is achieved using a coherent driving field, which leads to narrow amplification resonances. Using this approach, it is possible to obtain essentially pure two-photon amplification by adjusting the drive laser frequency slightly away from the atomic transitions to separate the frequency of the one- and two-photon amplification resonances, while enhancing the two-photon emission rate via resonance enhancement.

These two-photon amplification and lasing schemes are

different from the conceptually simplest scheme where amplification occurs through coupling of the field with an effective two-level atomic system (or with a three-level atomic system with a far-off-resonance intermediate level) that is pumped by means of an incoherent mechanism [8,9]. In the experiments, the pump energy is provided by a driving field through a coherent multiphoton process where two photons from the drive field are absorbed and, simultaneously, the probe (or lasing) field stimulates the emission of two additional probe (or lasing) photons. In spite of this difference, the properties of the light generated by both schemes are expected to share common features owing to the common quadratic dependence on the probe (or lasing) field intensity. In fact, it was shown theoretically [10] that the set of equations describing the experimental system used in Ref. [13] is isomorphic, in certain operating conditions, with that describing the incoherently pumped three-level atomic system. However, there are features unique to the coherently driven system, such as some coherence and saturation effects.

Another difference between the experiments with potassium atoms and the ideal incoherently pumped system is that more atomic levels are involved in the experimental scheme. As seen in Fig. 1, the fields interact with magnetic sublevels (with quantum numbers M_F , where F stands for the total atomic angular momentum) so that a relatively large number of levels are involved in the atom-field interaction processes. This richness has the drawback that it makes a theoretical description of the interactions more complex. However, it also opens up possibilities since it can lead to interference effects between different quantum pathways contributing to the same amplification process, and it allows for the appearance of higher-order amplification processes. Preliminary theoretical results reported in [17], obtained with a simplified model where part of the atomic sublevel manifold was ignored (and thus several multiphoton processes and coherence

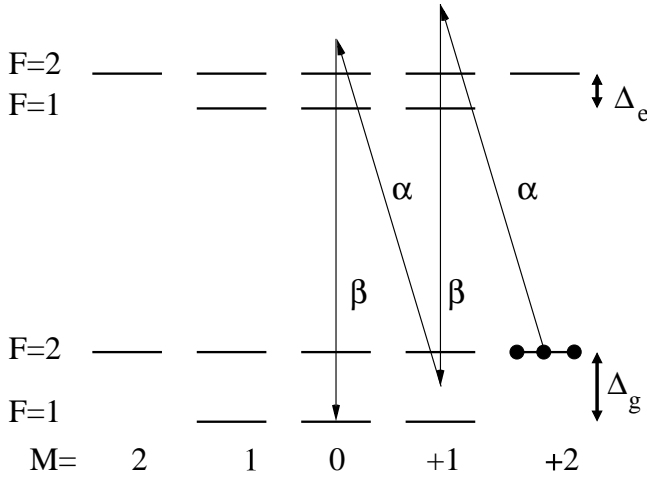


FIG. 1. Atomic energy levels ($\Delta_g/\Lambda=37.43$ and $\Delta_e/\Lambda=4.677$ for ^{39}K). The process giving rise to two-photon amplification of the probe field β is shown.

effects could not be described), clearly show this richness of phenomena.

In this paper we investigate theoretically the detailed behavior of such a coherently driven atomic system in an *amplification* configuration similar to that described in Ref. [16], where a beam of alkali-metal atoms is simultaneously irradiated by “driving” and a “probe” electromagnetic fields of arbitrary intensities. Our aim is to investigate the different coherent multiphoton processes involving amplification of the probe field that can take place owing to the richness of the atomic level structure, paying special attention to the two-photon amplification processes. To this end we will establish a semiclassical model that takes into account most of the essential factors that play a role in the amplification processes. In particular, it accounts for most of the hyperfine sublevels involved in the atom-field interaction (which allows us to study phenomena such as quantum-pathway interferences) as well as for the corresponding atomic relaxation rates and the finite interaction time between each atom and the electromagnetic fields. Thus, the present model extends the results of Ref. [17] by taking into account all possible multiphoton processes and coherence effects so that, for example, the drive- and probe-induced light shifts can be properly investigated. The only limitations of the model are the neglect of some broadening mechanisms such as the spatial nonuniformity of the fields and atomic beam and the possible residual Doppler broadening of the atomic beam. The influence of different control parameters is studied in detail.

The paper is organized as follows. In Sec. II, we describe the atom-field interaction and our model. In Sec. III, the different multiphoton resonances are analyzed, emphasizing the two-photon amplification resonance. Finally, the main conclusions are summarized and an outlook is given in Sec. IV.

II. MODEL

We consider two laser beams interacting with the ^{39}K $4S_{1/2} \leftrightarrow 4P_{1/2}$ transition as shown diagrammatically

in Fig. 1, which is the case investigated experimentally in Ref. [16]. Note that the theoretical development also applies to any alkali-metal atom with nuclear spin $I=3/2$. The ground-level manifold is composed of states $|g, F, M\rangle$, where $F=1, 2$ is the total angular momentum quantum number and M_F (to be denoted in the following simply as M) represents its projection on the quantization axis z . In a similar way, the excited-level manifold is composed of states $|e, F, M\rangle$. In each level, the $F=1$ and $F=2$ submanifolds are separated in energy by an amount $\hbar\Delta_g$ and $\hbar\Delta_e$, respectively. For ^{39}K , $\Delta_g/\Delta_e \approx 8$ (see Fig. 1 caption). As in Ref. [16], we assume that the atomic beam propagates in the x direction and that an optical pumping mechanism prepares most atoms ($\approx 95\%$ in the experiments of [16]) in the specific ground state $|g, 2, 2\rangle$. Two plane-wave fields of arbitrary intensity are incident on the atomic beam: a $\hat{\sigma}_-$ -polarized “drive” field $\hat{E}_d(z, t) = \{\hat{e}_- E_d \exp[i(k_d z - \omega_d t)] + \text{c.c.}\}/2$ propagating in the z direction, and a \hat{z} -polarized “probe” field $\hat{E}_p(y, t) = \{\hat{e}_z E_p \exp[i(k_p y - \omega_p t - \varphi_p)] + \text{c.c.}\}/2$ propagating in the y direction. The driving field couples with transitions $|g, F, M\rangle \leftrightarrow |e, F', M-1\rangle$ for any allowed value of F, F' , and M , whereas the probe field interacts with transitions $|e, F, M\rangle \leftrightarrow |g, F', M\rangle$.

In the usual rotating-wave, slowly-varying-envelope, and uniform-field approximations [18–20], the semiclassical density-matrix equations describing the evolution the atomic state can be expressed as

$$\dot{\rho}_{ii}(t) = \lambda_i - \left[\sum_j \gamma_{ji} + \gamma_{out} \right] \rho_{ii}(t) + \sum_j \gamma_{ij} \rho_{jj}(t) + \mathcal{F}_{ii} \{ \rho_{ij}(t), \beta_{ij}(t), \dot{\varphi}(t); \alpha_{ij}, \Delta_d, \Delta_p \}, \quad (1)$$

$$\dot{\rho}_{ij}(t) = -\Gamma_{ij} \rho_{ij}(t) - \mathcal{F}_{ij} \{ \rho_{ii}(t), \rho_{jj}(t), \beta_{ij}(t), \dot{\varphi}(t); \alpha_{ij}, \Delta_d, \Delta_p \},$$

where the density-matrix elements ρ_{ii} and ρ_{ij} represent the population of state $i \equiv |n, F, M\rangle$ (with n denoting g or e) and the slowly varying envelope of the atomic coherence induced on the transition between states i and j , respectively. The first term of the first equation gives the rate of injection of atoms with internal state i into the region of interaction with the incident fields; if the total injection rate is denoted as λ_0 , then $\lambda_0 = \sum_i \lambda_i$, so that λ_i/λ_0 is the fraction of atoms injected into state i . The parameter $\gamma_{out} = 1/\Delta t$ (where Δt is the averaged interaction time of the atoms with the fields) in the second term takes into account the fact that this interaction time is finite. The density matrix has been normalized initially to one atom so that $\lambda_0 = \gamma_{out}$. In all of the calculations, we have neglected the contribution of the different resonances involving sublevels with $M = -2$, since they can be reached only by high-order multiphoton processes from the initially populated sublevel $|g, 2, 2\rangle$, or by lower-order multiphoton processes initiated from other (much less populated) intermediate sublevels. Nevertheless, relaxation rates from $|e, 2, -1\rangle$ and $|e, 1, -1\rangle$ toward $|g, 2, -2\rangle$ have been taken into account, thus making the active medium an “open” sys-

tem. Thus, $\sum_i \rho_{ii}$ is less than 1 for later times, but is close to 1 for all conditions considered in our investigation.

The populations and coherences are affected by relaxation mechanisms, characterized by γ_{ji} for the population transfer rate from state i to state j , and $\Gamma_{ji} = \gamma_{out} + (\sum_k \gamma_{ki} + \sum_k \gamma_{kj})/2$ for relaxation of the coherence $\rho_{ij}(t)$. The main population relaxation mechanism is spontaneous emission from the excited to the ground states. Our model also includes rates for possible population transfer between ground states, which, for instance, might approximately account for the effects of optical pumping fields when such fields act simultaneously with the driving and probing fields. Nevertheless, in our calculations we will assume that optical pumping is performed just before the atoms enter the interaction region, as in the experiments of [16]. The effect of collisions between atoms on the coherence relaxation rates can be neglected [16]. The rates γ_{ij} corresponding to spontaneous emission have been calculated from the Clebsch-Gordan coefficient associated with each specific transition [21] and are given by $\gamma_{ij} = (\Lambda |\chi_{ij}|^2)$ with $\Lambda = (16\pi^3 \mu_0^2)/(3h\epsilon_0 \lambda^3)$ and

$$\begin{aligned} \chi_{ij} &= \langle (J' I') F' M' | \hat{T}_q | (J I) F M \rangle \\ &= (-1)^{F'-M'} \begin{pmatrix} F' & 1 & F \\ -M' & q & M \end{pmatrix} \delta_{I' I} (-1)^{J'+I+F+1} \\ &\quad \times \sqrt{(2F+1)(2F'+1)} \begin{Bmatrix} J' & I & F' \\ F & 1 & J \end{Bmatrix}, \end{aligned} \quad (2)$$

where I and J represent the nuclear and angular momentum, respectively, and \hat{T}_q is the electric dipolar operator [$q = -1, 0, 1$, depending on the polarization(s) of the field(s) considered in each transition]. In Eq. (2), the ‘‘primed’’ quantities refer to the upper state of the specific transition considered. The parameters are the matrix element $\langle J', S, L' | \hat{T} | J, S, L \rangle = \mu_0 = 4.23ea_0 = 3.58 \times 10^{-29}$ C m, ϵ_0 is the vacuum permittivity, and λ is the wavelength of the transition (769.9 nm for ^{39}K). From Eq. (2), the values of the dimensionless factors χ_{ij} , which obey $\chi_{ij} = \chi_{ji}$, are given by

$$\begin{aligned} \chi_{e22,g22} &= \chi_{e10,g20} = \chi_{e20,g10} = \sqrt{6}/6, \\ \chi_{e22,g11} &= -\chi_{e11,g22} = -\chi_{e1-1,g2-2} = 1/2, \\ \chi_{e21,g22} &= -\chi_{e22,g21} = -\chi_{e2-1,g2-2} = \sqrt{3}/6, \\ \left. \begin{aligned} \chi_{e11,g21} &= \chi_{e21,g11} = \chi_{e21,g10} \\ \chi_{e20,g21} &= \chi_{e1-1,g2-1} = \chi_{e2-1,g20} \\ \chi_{e2-1,g10} &= \chi_{e2-1,g1-1} \end{aligned} \right\} &= \sqrt{2}/4, \quad (3) \\ \left. \begin{aligned} \chi_{e21,g20} &= \chi_{e10,g21} \\ \chi_{e10,g2-1} &= \chi_{e20,g2-1} \end{aligned} \right\} &= -\sqrt{2}/4, \\ \left. \begin{aligned} \chi_{e11,g10} &= \chi_{e21,g21} = \chi_{e10,g1-1} \\ \chi_{e20,g11} &= \chi_{e20,g1-1} = \chi_{e1-1,g1-1} \end{aligned} \right\} &= \sqrt{6}/12, \end{aligned}$$

$$\begin{aligned} \left. \begin{aligned} \chi_{e11,g20} &= \chi_{e11,g11} = \chi_{e10,g11} \\ \chi_{e1-1,g20} &= \chi_{e1-1,g10} = \chi_{e2-1,g2-1} \end{aligned} \right\} &= -\sqrt{6}/12, \\ \chi_{e10,g10} &= \chi_{e20,g20} = 0. \end{aligned}$$

The functions \mathcal{F}_{ij} and \mathcal{F}'_{ij} in the last term of each equation in (1) arise from the quantum Liouville evolution commutator and represent the effect of the incident coherent fields on the atomic state. Some of these functions are given in the Appendix. They depend on the atomic parameters described above as well as on the interaction strengths of the fields with each transition, which are characterized by the Rabi frequencies

$$2\alpha_{ij} = \frac{\mu_{ij} E_d}{\hbar}, \quad 2\beta_{ij} = \frac{\mu_{ij} E_p}{\hbar} \quad (4)$$

of the drive and probe fields, respectively, where $\mu_{ij} = \mu_0 \chi_{ij}$ is the electric-dipole matrix element of transition ij . In the discussion below, we also make use of an *averaged* value of the Rabi frequency, which we define as $2\alpha = \mu_0 E_d / \hbar$ for the drive field and $2\beta = \mu_0 E_p / \hbar$ for the probe field, so that $2\alpha_{ij} = 2\alpha \chi_{ij}$ and $2\beta_{ij} = 2\beta \chi_{ij}$. The detuning of the drive field with respect to the optical transitions is controlled by the parameter $\Delta_d = \omega_d - \omega_{e2-g1}$, where ω_{e2-g1} is the frequency of the transition $|e, 2, M\rangle \leftrightarrow |g, 1, M\rangle$ for any M and $\Delta_p = \omega_p - \omega_d$ controls the difference between the probe and drive-field frequencies.

We determine the populations of each level and the atomic coherences that are created in the interaction region by numerically integrating Eqs. (1), taking into account both the continuous feeding and loss of atoms from the region and the action of the fields. The density-matrix elements correspond to an average over all atoms present in the interaction region at a given instant. Note that such averaging is performed through the atomic injection (λ_i) and expulsion (γ_{out}) rates [see Eqs. (1)] rather than by calculating the internal-state evolution of each atom as a function of the exact time it is injected into and expelled from the interaction region. Our procedure is simpler and is known to give the same steady-state results for this type of problem.

From the numerical solution of Eqs. (1), it is possible to determine a complex ‘‘gain’’ $\tilde{G} \equiv -\omega_p \Delta n - iG$ for the probe field, given by

$$\tilde{G} = \frac{U}{\beta} \left[\sum_{F, F'} \sum_M \chi_{gF'M, eFM} \rho_{eFM, gF'M} \right], \quad (5)$$

where $U = N \omega_p \mu_0^2 / 2\epsilon_0 \hbar$ represents the unsaturated gain parameter, N is the density of atoms in the interaction region, and the summation extends to all the one-photon atomic coherences induced on the transitions $|e, F, M\rangle \rightarrow |g, F', M\rangle$. The imaginary part of Eq. (5), or the *gain factor* G , represents the relative increase in the probe-field amplitude per unit of time (so that the relative increase in the probe-field *intensity* is given by $2G$). The real part of Eq. (5) is the product $-\omega_p \Delta n$, where Δn is the change in the refractive index of the atomic medium at the probe-field frequency

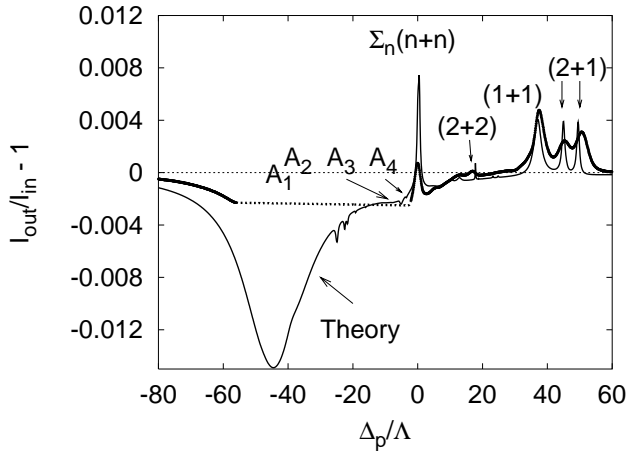


FIG. 2. Thin continuous line: relative intensity gain as a function of the probe detuning for $\alpha/\Lambda=12, \beta/\Lambda=12$, drive-field detuning $\Delta_d/\Lambda=4.86$, $\lambda_0/\Lambda=\gamma_{out}/\Lambda=0.07$, $(U/\Lambda^2)\Delta y=60$ m, and a 94% efficient initial optical pumping to state $|g,2,2\rangle$ (with a residual initial population of 1% at each one of the six remaining ground-level states) has been assumed. The experimental results [16] (thick line) are also shown for comparison. Note that the experimental recording is invalid because of detector saturation from $\Delta_p/\Lambda=-55$ to -5 (thick dotted line).

brought about by the simultaneous action of the drive and probe fields on the atoms. In what follows, we mostly focus on the study of the gain factor G , although the real part of the gain can also be important since, for instance, it gives the “frequency pushing” effect that appears when the atomic medium is placed inside an optical cavity.

Throughout the paper, all quantities with dimensions of s^{-1} (including gains \tilde{G} and G) are converted to dimensionless form by normalizing them by $\Lambda=7.75\times 10^7 s^{-1}$. Consistent with this normalization, time must be multiplied by Λ and U must be divided by Λ^2 .

III. RESULTS: MULTIPHOTON PROCESSES

In this section we present results of the probe-beam gain calculated according to Eqs. (1) and (5), for parameter settings reproducing as closely as possible the experimental conditions of Refs. [16,17], and also for other parameter settings. Only values corresponding to steady-state atomic fluxes and field intensities are given. First, we make a comparison with the experimental results of [16], and in the rest of the section we analyze the properties of the multiphoton resonances.

The thick line in Fig. 2 shows the experimental gain $I_{out}/I_{in}-1$ as a function of the probe detuning Δ_p/Λ , as measured in [16]. I_{in} and I_{out} represent the injected and output probe-field intensities, respectively. The drive detuning with respect to the associated atomic transitions is relatively large in this case: from $\sim 47\Lambda$ for transitions $|g,2,M\rangle \rightarrow |e,1,M-1\rangle$ to $\sim 5\Lambda$ for transitions $|g,1,M\rangle \rightarrow |e,2,M-1\rangle$. This difference separates the different multiphoton processes in frequency. The thinner-line curve shows the same physical quantity, calculated from our theoretical

model for a fixed parameter setting, assuming $I_{out}/I_{in}-1=2G\Delta y/c$, where G is determined from Eq. (5), Δy is the effective atomic-beam diameter in the direction of propagation of the probe beam, and c is the speed of light in the medium. Hence, $\Delta y/c$ is the probe-beam interaction time. A product $(U/\Lambda^2)\Delta y=60$ m has been considered, which can be achieved with an atomic beam of effective density N near 10^{17} atoms/m³ and effective diameter $\Delta y\approx 2\times 10^{-3}$ m.

The first remarkable feature seen in Fig. 2 is the good agreement between experiment and theory. The positions of the gain (and absorption) resonances are coincident and the peak strengths are of the same order of magnitude. This allows us to confirm the origin of each gain resonance, as will be discussed below. The differences in the line strengths and widths are due to factors neglected in our model (the spatial profiles of the fields and atomic beam, the broadening induced by residual Doppler effect), and experimental uncertainties in the atomic-beam parameters, field intensities, interaction time of each atom with the fields, and optical pumping details. In fact, there is a domain of values of the atom interaction time γ_{out}^{-1} , for which results close to the experimental ones are obtained. We have checked that an increase of up to a factor of 4 in γ_{out} still leads to good results.

In the rest of this section, we will study the influence of the main physical parameters on the different resonances. We will start with the absorption dip and continue with each gain resonance, from that corresponding to the lowest-order multiphoton process to that corresponding to the highest-order one. Although we are especially interested in the two-photon amplification resonance, we will also discuss some properties of other multiphoton resonances since they might be useful for certain applications and their comparison will help us gain a deeper understanding of the multiphoton processes.

Absorption resonances A_i . The large absorption dip appearing in Fig. 2 at negative detunings corresponds to the overlap of two pairs of probe absorption resonances. Pair A_1 and A_2 corresponds to transitions $|g,2,M\rangle \rightarrow |e,i,M\rangle$, with $i=1$ and 2 , respectively, occurring at $\Delta_p/\Lambda \approx -(\Delta_d+\Delta_g+\Delta_e)/\Lambda=-45.8$, and $\Delta_p/\Lambda \approx -(\Delta_d+\Delta_g)/\Lambda=-41.3$, respectively. The strongest contribution is, by far, that of the transition $|g,2,2\rangle \rightarrow |e,2,2\rangle$, because of the largest population of the initial level (see Fig. 2 caption). The second pair A_3 and A_4 corresponds to transitions $|g,1,M\rangle \rightarrow |e,i,M\rangle$ for $i=1$ and 2 , respectively, and appear at $\Delta_p/\Lambda \approx -(\Delta_d+\Delta_e)/\Lambda=-9.3$ and $\Delta_p/\Lambda \approx -\Delta_d/\Lambda=-4.7$. This pair of resonances is much weaker since none of them involves the initially most populated state $|g,2,2\rangle$. Nevertheless, the experimental curve in Fig. 2 suggests that these resonances are larger than predicted by our model.

We believe that the discrepancy in the size of the absorption peaks is due to the fact that the drive laser beam is significantly larger than the probe laser beam in the experiment ($250 \mu\text{m}$ in comparison to $90 \mu\text{m}$), whereas we assume they are the same size in our model. Hence, the atoms will be optically pumped out of the initial state $|g,2,2\rangle$ by the intense drive field to a larger extent in the experiment in comparison to our model. The greater depletion of the initial state increases the strength of the absorption resonances and

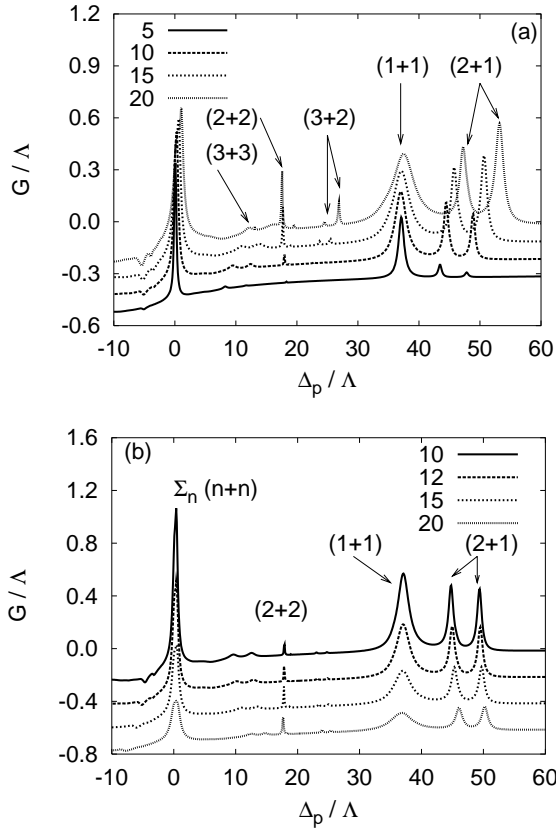


FIG. 3. Gain G , as given by Eq. (5), as a function of probe-drive detuning Δ_p/Λ . In (a) a probe amplitude of $\beta/\Lambda = 12$ and different drive amplitudes are shown (for the sake of clarity, curves corresponding to $\alpha/\Lambda = 5, 10$, and 15 have been shifted down by $0.3, 0.2$, and 0.1 units, respectively); in (b) a drive amplitude of $\alpha/\Lambda = 12$ and different probe amplitudes are depicted (curves corresponding to $\beta/\Lambda = 12, 15$ and 20 have been shifted down by $0.2, 0.4$, and 0.6 units, respectively). Other parameters as in Fig. 2 (in particular, $\Delta_d/\Lambda = 4.87$), with $U/\Lambda^2 = 3000$ and $\gamma_{out}/\Lambda = 0.07$.

decreases the strength of the gain resonances somewhat. We have verified that a wider and deeper absorption dip closer to that of the experimental results of Fig. 2 can be obtained by changing the initial populations of the ground-level states in our model.

Since we are interested in amplification, the most important consequence of the presence of the large absorption dip in Fig. 2 is that its blue wing (which extends up to very large values of Δ_p) can reduce the strength of the closest multiphoton amplification resonances. In particular, it represents one of the main physical obstacles for efficient two-photon amplification and lasing [16,7].

Amplification resonances. The gain peaks of Fig. 2, which are reproduced in more detail in Fig. 3 for several values of the drive- [Fig. 3(a)] and probe- [Fig. 3(b)] beam Rabi frequencies, correspond to different multiphoton coherent processes. Each process is denoted as an $(n+m)$ -photon process, which involves absorption of n drive photons and simultaneous emission of m probe photons in an alternating way [see, for instance, the $(2+2)$ -photon process depicted in Fig. 1]. Of such processes, only those starting at the initially

most populated atomic state $|g, 2, 2\rangle$ are more clearly perceptible in Figs. 2 and 3. Their locations (ignoring for the moment any possible light-induced shift), as well as the initial and final atomic states they connect, are given in Table I.

We first discuss general features of these multiphoton processes, and then we will consider specific aspects of each one of them. The first general feature to point out is that, as expected, the peak gain G associated with these multiphoton resonances increases, for relatively weak drive and probe fields, proportionally to α^{2n} (i.e., the intensity of the drive beam raised to the power n) and to $\beta^{2(m-1)}$ (i.e., the probe-beam intensity raised to the power $m-1$). For higher intensities, saturation slows down the growth process, as can be seen easily for the $(1+1)$ -photon resonance in Fig. 3(a), for example. This behavior is illustrated in Figs. 4(a) and 4(b) for several of the $(n+m)$ -photon resonances; further details are given below.

A second general feature is that the gain resonances undergo radiative shifts due to the ac-Stark effect when the drive or probe intensities become large. These shifts, for a given resonance, can be viewed as due to the radiative shifts of the initial and final states of the corresponding multiphoton process, brought about by the drive or probe fields through their coupling with any optical transition involving such an initial or final state. For the case when $\beta \ll \alpha$ and $\alpha \ll \Delta_{djk}$ for all jk , where $\Delta_{djk} = \omega_d - \omega_{jk}$ is the detuning of the drive field from the $j \leftrightarrow k$ transition, the radiative shift of an $(n+m)$ multiphoton resonance between initial state i and final state f is given by

$$\delta_{fi} = \frac{1}{m} \left[-(-1)^{n+m} \sum_r \frac{|\alpha_{rf}|^2}{\Delta_{drf}} + \sum_s \frac{|\alpha_{si}|^2}{\Delta_{dsi}} \right], \quad (6)$$

where the sum of the first (second) term describes the ac-Stark shift of the final (initial) state $f(i)$, which is defined as positive when it is an upward shift. Equation (6) has been obtained by adapting expressions from Ref. [22] to our light-atom interaction configuration. For large probe and drive Rabi frequencies, Eq. (6) becomes less reliable.

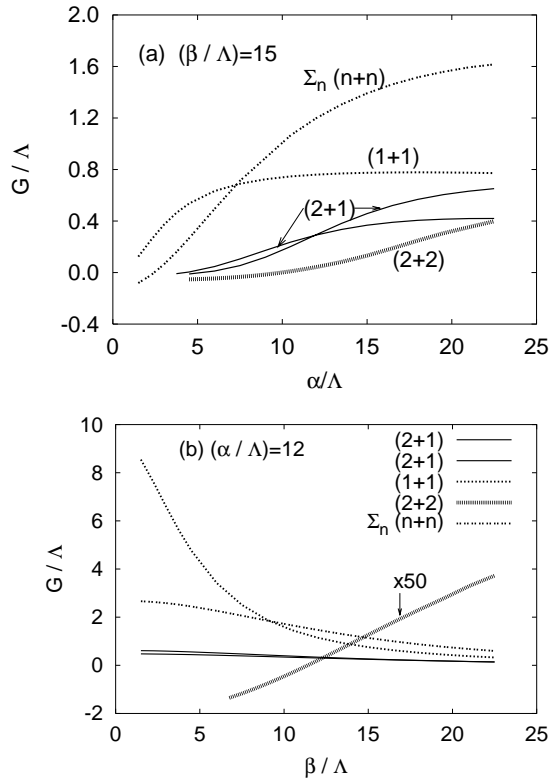
An analysis with Eq. (6) for the data shown in Fig. 3 reveals the following set of general rules that apply to the positions of all gain resonances.

(i) With increasing drive amplitude [Fig. 3(a)], all gain peaks corresponding to $(n+m)$ -photon processes with $n = m$ [namely, $(1+1)$ -, $(2+2)$ -, and $(3+3)$ -photon processes] undergo very small shifts, whereas those processes with $n \neq m$ [namely, $(2+1)$ - and $(3+2)$ -photon processes] undergo strong blueshifts. The reason for this behavior is as follows: in the $n = m$ processes, the initial and final atomic states of the process (Table I, second column) are both ground-level states and undergo similar drive-induced light shifts, since the drive field couples to manifolds possessing excited states having M one unit smaller in both cases. This leaves the resonance position almost unchanged with respect to the unshifted position (Table I, third and fourth columns).

In contrast, for the $(n+m)$ -photon processes with $n \neq m$, the final atomic state belongs to the *excited*-level manifold, which undergoes a drive-induced shift that is opposite to the shift experienced by the initial state. Due to this effect,

TABLE I. Multiphoton gain processes involving absorption of n drive photons and emission of m probe photons. Light shifts have been ignored in the last two columns.

$(n+m)$ -photon process	Initial and final states	Unshifted resonance position Δ_p	
		Generic position	In Fig. 3
(1+1)	$ g,2,2\rangle \xrightarrow{\alpha\beta} g,1,1\rangle$	$\Delta_p = \Delta_g$	37.4
(2+1)	$ g,2,2\rangle \xrightarrow{\alpha\beta\alpha} e,2,0\rangle$	$\Delta_p = \Delta_g + \Delta_d$	42.3
	$ g,2,2\rangle \xrightarrow{\alpha\beta\alpha} e,1,0\rangle$	$\Delta_p = \Delta_g + \Delta_d + \Delta_e$	47.0
(2+2)	$ g,2,2\rangle \xrightarrow{\alpha\beta\alpha\beta} g,1,0\rangle$	$\Delta_p = \Delta_g/2$	18.7
(3+2)	$ g,2,2\rangle \xrightarrow{\alpha\beta\alpha\beta\alpha} e,2,-1\rangle$	$\Delta_p = (\Delta_g + \Delta_d)/2$	21.15
	$ g,2,2\rangle \xrightarrow{\alpha\beta\alpha\beta\alpha} e,1,-1\rangle$	$\Delta_p = (\Delta_g + \Delta_d + \Delta_e)/2$	23.5
(3+3)	$ g,2,2\rangle \xrightarrow{\alpha\beta\alpha\beta\alpha\beta} g,1,-1\rangle$	$\Delta_p = \Delta_g/3$	12.5
	$ g,2,2\rangle \xrightarrow{\alpha\beta} g,2,1\rangle$		
$\sum_{n=1}^3 (n+n)$	$\xrightarrow{\alpha\beta} g,2,0\rangle$	$\Delta_p = 0$	0
	$\xrightarrow{\alpha\beta} g,2,-1\rangle$		


 FIG. 4. Evolution of the $(n+m)$ -photon gain resonance strengths with the drive (a) and probe (b) amplitudes. The rest of the parameters are the same as in the previous figure, except for $\gamma_{out} = 0.3$. Note that, for the sake of clarity, the gain strength for the (2+2)-photon resonance has been multiplied by 50 in (b).

we find that the multiphoton gain resonance undergoes a shift that, in the limit of low probe amplitude, is the sum of the drive-induced light shifts of the initial and final states (see Table I, second column), divided by m . The shift is to higher energies in Fig. 3 since the drive-field detuning Δ_d is positive; it brings about an upward (downward) shift of the initial (final) state of the multiphoton process.

(ii) With increasing probe amplitude [Fig. 3(b)], all gain peaks corresponding to $(n+m)$ -photon processes with $n=m$ [namely, (1+1)-, (2+2)-, and (3+3)-photon processes] undergo a small redshift in general, whereas those processes with $n \neq m$ [namely, (2+1)- and (3+2)-photon processes] undergo a relatively large blueshift for reasons similar to those discussed above in point (i), considering now the probe-induced light shift of the final state of each multiphoton process. For the case of the (2+2) peak, it will be shown below that the small shift can be to the blue side instead of to the red side for large values of the probe-field amplitude.

We note that most of these shifts in the multiphoton resonances could not be correctly described with the simplified model of Ref. [17] since the coupling of the drive and probe fields with transitions involving levels with $M < 0$ were ignored.

(iii) Finally, a third general feature is the existence of several quantum pathways connecting the initial and final atomic states for each $(n+m)$ -photon process. The multiple pathways arise from the existence of two ground states and two excited states for each value of M (corresponding to the two possible values of F), which implies that *two* real atomic levels exist at each intermediate step of any $(n+m)$ -photon process. This leads to quantum interference

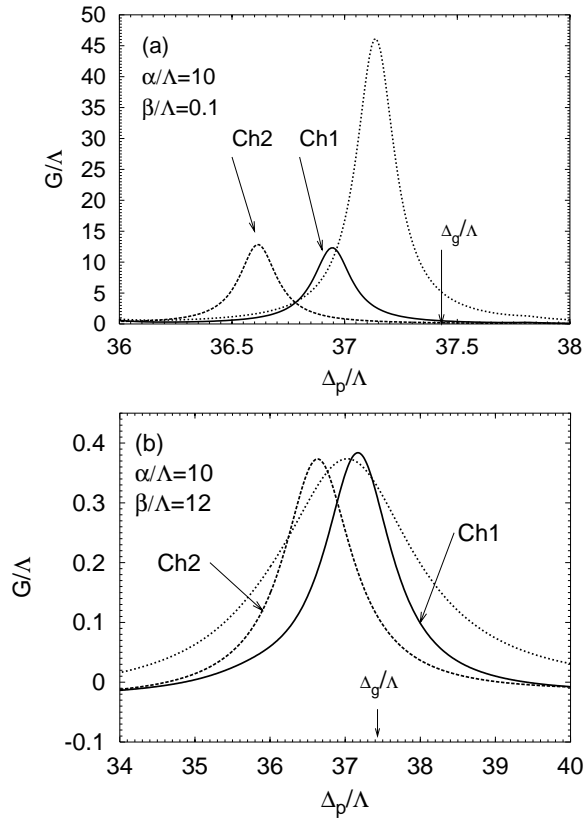


FIG. 5. Probe-beam gain as a function of Δ_p showing different quantum paths for the Raman (1+1)-photon feature, demonstrating their constructive interference. (a) The probe field β is weak compared to the drive field α . (b) Both fields are intense. Other parameters are the same as in Fig. 3.

phenomena between these pathways, which affect both the strength and position of the $(n+m)$ -photon gain resonances. The interference can be either constructive or destructive depending on the signs of the matrix elements [Eq. (3)] contributing to each pathway and of the associated field detunings.

We consider below specific features of several of the multiphoton processes, and discuss in particular the interference effects between quantum channels. We start with the (1+1)-photon process, which, because of its simplicity, will allow us to easily analyze details of such interference effects.

(1+1)-photon Raman process

The availability of two intermediate states for the Raman process (namely, states $|e,2,1\rangle$ and $|e,1,1\rangle$), leads to the existence of two quantum paths connecting the initial state $|g,2,2\rangle$ with the final state $|g,1,1\rangle$. Figure 5(a) shows, for a case of strong drive ($\alpha=10$) and weak probe ($\beta=0.1$), the Raman peak position in several possible situations: channel 1 (ch1) corresponds to a case where only one of the two intermediate states, namely, state $|e,1,1\rangle$, is present (i.e., we have canceled all the field couplings with state $|e,2,1\rangle$, keeping all the rest of the interactions with atomic states active, in particular, the process $|g,2,2\rangle \rightarrow \alpha|e,1,1\rangle \rightarrow \beta|g,1,1\rangle$); channel 2 (ch2) corresponds to the opposite case with only the interme-

diated state $|e,2,1\rangle$ (i.e., excluding now couplings with state $|e,1,1\rangle$), and considering, in particular, the process $|g,2,2\rangle \rightarrow \alpha|e,2,1\rangle \rightarrow \beta|g,1,1\rangle$); and channel 1+2 [ch(1+2)] corresponds to the actual case where both intermediate levels exist. The unshifted location of the resonance, for which the ac-Stark shifts are not taken into account ($\Delta_p = \Delta_g$), is pointed out on the horizontal axis.

It is clearly seen in Fig. 5(a) that there is constructive interference between ch1 and ch2. Quantitative analysis of the data shown in the figure reveals the following aspects of the (1+1)-photon resonance. It is seen that the gain strength for channel 2 is slightly larger than for channel 1. This is due to the fact that the dipole matrix coefficients for ch1 (product $\chi_{g22,e11}\chi_{e11,g11}$) and ch2 (product $\chi_{g22,e21}\chi_{e21,g11}$) have precisely the same value, while the value of the drive detuning is slightly smaller for ch2 than it is for ch1 (42.3 vs 47.0). Furthermore, for ch(1+2), we find that the corresponding gain peak strength is given approximately by $(\sqrt{G_1} + \sqrt{G_2})^2$, where G_i ($i=1,2$) represents the gain peak strength for channel i . If the probe-field intensity is increased to a larger value, such as that shown in Fig. 5(b), the agreement with this relation is only qualitative because of saturation effects.

The observed shifts of the resonance in Fig. 5(a) are small due to the fact that the ac-Stark shifts of the initial $|g,2,2\rangle$ and final $|g,1,1\rangle$ states involved in the scattering process are of the same sign and similar strength, as pointed out above. According to Eq. (6), the final state shifts upward by an amount of 1.3Λ , and at the same time the initial state $|g,2,2\rangle$ also shifts upward by amounts of 0.5Λ (for ch1), 0.2Λ (for ch2), and $(0.5+0.2)\Lambda$ [for ch(1+2)]. The larger shift of the final state is due to the much smaller detuning of the drive field with respect to transitions $|g,1,1\rangle \leftrightarrow |e,F,0\rangle$ (for $F=1,2$) as compared to transitions $|g,2,2\rangle \leftrightarrow |e,F,1\rangle$ (9.5Λ and 4.9Λ vs 47.0Λ and 42.3Λ , respectively), which compensates for the smaller dipole matrix coefficients associated with transitions $|g,1,1\rangle \leftrightarrow |e,F,0\rangle$. This implies that the peak-position shifts are all negative in Fig. 5(a). Nevertheless, the values of such negative shifts measured from the exact (numerically calculated) curves in Fig. 5(a) are 0.3Λ units (in absolute value) smaller than the values predicted by Eq. (6) in all three cases. This deviation is due to the overestimation, by Eq. (6), of the $|g,1,1\rangle$ state upshift, owing to the fact that the drive detuning with respect to transition $|g,1,1\rangle \leftrightarrow |e,2,0\rangle$ (which is equal to 4.9Λ) is not small enough for such an equation to be exact [22].

It is worth emphasizing that there is constructive interference between channels 1 and 2 in the case considered in Fig. 5(a) because the products of the two electric-dipole matrix elements involved in each channel (see above) have the same sign, and the drive-field detuning also has the same sign for both channels. But in other cases not satisfying these conditions, destructive interferences can occur. Such destructive interferences can even completely cancel a given gain resonance. Figure 6 illustrates such behavior by considering two cases with a drive field very close to resonance with the atomic transitions. For the sake of clarity, relatively small values of the drive and probe amplitudes have been consid-

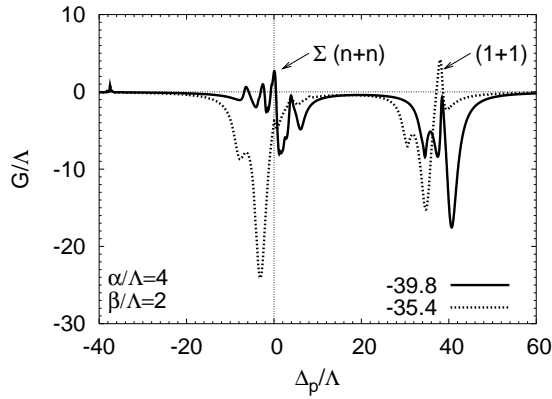


FIG. 6. Probe-beam gain as a function of Δ_p/Λ , for $\alpha/\Lambda=4$, $\beta/\Lambda=2$, and $\Delta_d/\Lambda=-39.8$ (continuous line) and -35.4 (dashed line); the remaining parameters are the same as in Figs. 3 and 5. Destructive quantum interference cancels either coherent process (1+1) at $\Delta_p/\Lambda=37.4$ (continuous-line curve) or coherent process $\Sigma_{n=1}^3(n+n)$ at $\Delta_p/\Lambda=0$ (dashed-line curve).

ered in the figures. The following features can be observed clearly.

(i) In the case of the continuous-line curve ($\Delta_d/\Lambda=-39.8$), the (1+1) Raman gain peak, which should appear at $\Delta_p/\Lambda=\Delta_g/\Lambda=37.4$, is canceled out. This occurs because the drive detuning with respect to the pump transition for ch1 and for ch2 takes the values $+2.3\Lambda$ and -2.3Λ , respectively, and thus there is a change of sign which entails destructive interference between the two channels. Note also that this gain destruction is reinforced by the quite strong probe absorption occurring at nearby values of Δ_p/Λ (see the strong dips near 37.4 in Fig. 6) associated with transitions $|g,1,1\rangle\rightarrow\beta|e,F,1\rangle$, for both $F=1$ and 2. Such absorption is in effect resonant for Δ_p/Λ near $-(\Delta_d+\Delta_e)/\Lambda=35.1$ and $-\Delta_d/\Lambda=39.8$, respectively, and is strong because the quasiresonant drive field pumps many atoms from the initial state $|g,2,2\rangle$ to the excited states $|e,F,1\rangle$, and from these states they decay very fast to ground states, in particular, to the state $|g,1,1\rangle$. Close inspection of the populations of states $|g,1,1\rangle$ and $|e,F,1\rangle$ as a function of Δ_p allows one to completely understand even the “fine structure” of the whole absorption dip appearing in the region of Δ_p/Λ between 30 and 45.

(ii) In the case of the dashed-line curve ($\Delta_d/\Lambda=-35.4$) in Fig. 6, the peak that usually exists at $\Delta_p/\Lambda=0$ now disappears, and the (1+1) Raman peak reappears. The peak at $\Delta_p/\Lambda=0$ corresponds to the process pointed out in Table I as $\Sigma_{n=1}^3(n+n)$ (further details about this process are given below). Since the drive and probe amplitudes are relatively small in Fig. 6, this process is actually dominated by its first step, i.e., a (1+1) process starting at state $|g,2,2\rangle$ and ending at state $|g,2,1\rangle$. Thus, it is also a Raman transition, but now the product of two electric-dipole matrix elements determining the associated transition probability takes a different value and a different *sign* for channels 1 and 2 of the process [see Eq. (3)]. This means that the drive detuning must have the same sign in both channels to observe destructive interference between them. This is in effect the case for

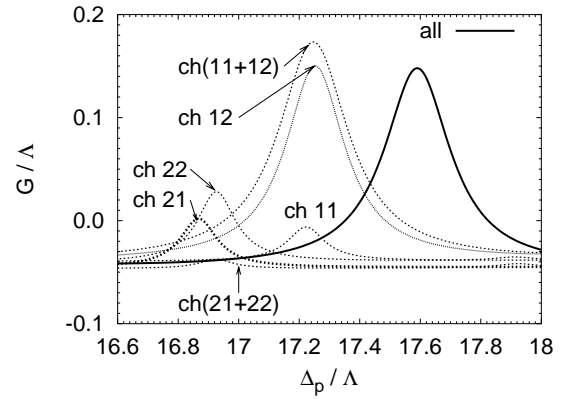


FIG. 7. Two-photon probe-beam gain for several of the possible quantum channels contributing to the (2+2)-photon process of Figs. 2 and 3 (for $\alpha/\Lambda=15, \beta/\Lambda=20$). Each channel is defined by the following atomic sublevels: $\text{Ch}FF': |g,2,2\rangle\rightarrow|e,F,1\rangle\rightarrow|g,F',1\rangle\rightarrow|e,2,0\rangle\rightarrow|g,1,0\rangle$. Channels 11+12 (21+22) give constructive (destructive) interference. The curve “all” (continuous line) has been calculated considering all possible atomic channels. Other parameters as in Fig. 3.

$\Delta_d/\Lambda=-35.4$ shown in Fig. 6, where the drive detuning with respect to the pump transition for ch1 and for ch2 takes the values $+6.7\Lambda$ and $+2.0\Lambda$, respectively. Estimating the transition probability for each channel indicates that we are very close to complete cancellation of the process for these values, as indeed is observed in Fig. 6.

Also apparent in Fig. 6 is a strong inhibition of the primary absorption resonance (i.e., the one caused by $|g,2,2\rangle\rightarrow\beta|e,2,2\rangle$) in the vicinity of $\Delta_p=0$. The absorption is suppressed by quantum interference between different coherent and incoherent (step-by-step) processes of different order. For example, (2+1) multiphoton resonance overlaps with the absorption resonance, even leading to net amplification as shown by the solid line in Fig. 6. Such absorption cancellation may be useful for removing one of the primary processes that makes it difficult to achieve two-photon lasing, as mentioned in the discussion of the absorption resonance A_i .

(2+2)-photon process

For the case of the (2+2)-photon process, the existence of several quantum channels also affects the strength and position of the gain resonance. As an example, Fig. 7 shows the (2+2)-photon gain resonance for several of the quantum pathways connecting the initial state $|g,2,2\rangle$ with the final state $|g,1,0\rangle$ (see figure caption). For instance, it can be seen that the quantum channel ch12 involving the intermediate states $|e,1,1\rangle$ and $|g,2,1\rangle$ yields larger gains than channels involving any other equivalent couplets of intermediate states, which is due to the fact that the product of the four Clebsch-Gordan coefficients involved in the gain expression is, according to Eqs. (3), three times larger for these states. On the other hand the signs of these Clebsch-Gordan coefficients determine whether the interference between each pair of channels will be constructive or destructive. In particular, it is constructive for ch(11+12), which is the superposition of ch11 and ch12, whereas it is destructive for ch(21+22).

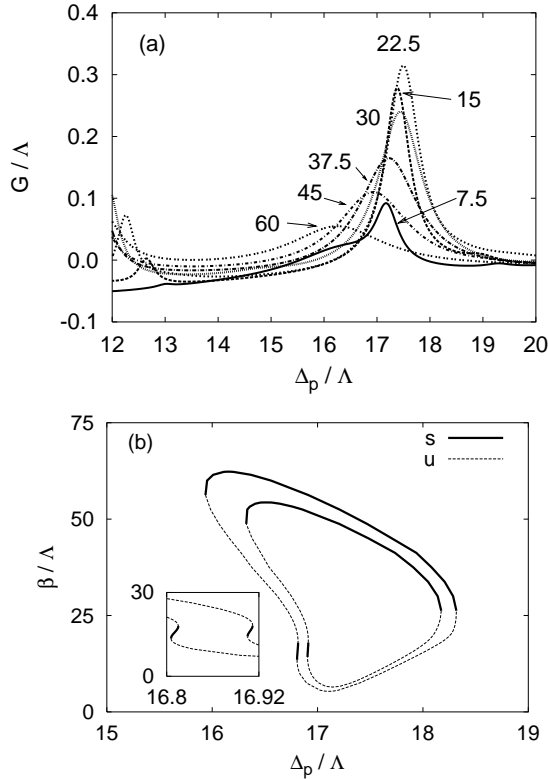


FIG. 8. (a) Gain for the (2+2)-photon resonance, for $\alpha/\Lambda = 18$ and different values of the probe amplitude β/Λ (from 7.5 to 67.5, in steps of 7.5), as a function of the probe-field detuning. Other parameters as in Fig. 3, except for $\gamma_{out}/\Lambda = 0.3$. (b) Amplitude of the field that would be delivered by a two-photon laser (stable emission, continuous line; unstable emission, dotted line) for a cavity with losses $\kappa = 0.05$ (outer curve) and $\kappa = 0.07$ (inner curve), as a function of the emitted-field detuning [other parameters as in (a)]. Each curve shows two stable regions delimited by vertical tangent lines. The smaller region is shown enlarged in the inset.

Finally, we also find that the gain peak position is different for each channel because they involve different ac-Stark shifts.

It is worth noting here that cancellation of the (1+1) coherent processes by quantum interference, as described in the previous section, can never imply destruction of the (2+2) resonance. This is because the two (1+1) processes discussed there contribute to different quantum channels for the (2+2) resonance, and hence there is no drive detuning for which these processes can be canceled simultaneously.

The fact that the (2+2)-photon process involves two probe photons and can be well separated from other gain or absorption resonances (see Fig. 3) makes it appropriate for two-photon amplification of the probe field and also for lasing. To better assess such possibilities, Fig. 8(a) shows an example of the evolution of the (2+2)-photon peak spectral profile for increasing values of the probe field strength β . Inspection of this figure shows two main features.

(i) With increasing β , the two-photon gain peak strength first increases proportionally to the probe intensity β^2 as expected for a process involving two probe photons, and then it decreases because of saturation. The maximum gain occurs,

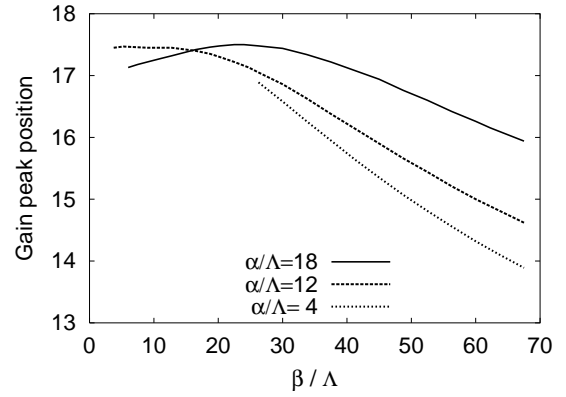


FIG. 9. Gain peak position (in units of Λ) for the (2+2)-photon resonance as a function of the probe amplitude β , for $\alpha/\Lambda = 4, 12$, and 18 (and $\gamma_{out}/\Lambda = 0.3$). The last case corresponds to that of Fig. 8(a). The unshifted position is at $\Delta_p = \Delta_g/2 = 18.7$. Note that the curve for $\alpha/\Lambda = 4$ ends around $\beta/\Lambda = 26$ because the gain resonance can no longer be distinguished for smaller values of β .

in the case considered in Fig. 8(a), for a value of β determined approximately through the relation $(\alpha\beta)/\Lambda^2 \approx 4 \times 10^2$. This is consistent with the fact that the probe saturation intensity for a (2+2)-photon process is given, in a simplified model where only a single quantum pathway and a single value of the drive and probe Rabi frequencies for all the transitions involved are taken into account, by [23]

$$\beta_{sat}^2 = \Gamma \Delta_1 \Delta_2 \Delta_3 / \alpha^2, \quad (7)$$

where Γ is the coherence decay rate between the initial and final states of the multiphoton process and Δ_i (for $i=1,2,3$) are the detunings of the intermediate virtual levels of the multiphoton process with respect to their respective atomic transitions (Fig. 1). Using values for these parameters similar to those considered in our calculations, and taking into account expressions (4), fair agreement with the saturation behavior shown in Fig. 8 is found for $\Gamma/\Lambda \approx 0.1$, which is a few times smaller than the upper-level population relaxation rates.

(ii) As pointed out above, increasing the probe amplitude when the drive-field amplitude is set to a moderate value leads to an increasing redshift of the gain resonance, as shown in Fig. 9 for $\alpha/\Lambda = 4$ and 12 . However, this is not always true for large drive amplitudes, as shown in Fig. 8(a) and Fig. 9 (solid line) for the case of $\alpha/\Lambda = 18$, where it is seen that there is a blueshift of the resonance when β is increased, for the regime when $\beta/\Lambda < 20$.

Figure 8(a) also provides useful information for predicting the behavior of a possible “two-photon laser” based on the (2+2)-photon amplification resonance. Consider a horizontal line crossing the vertical axis at a value determined by the loss rate of the laser cavity. The intersection of this line with the gain curves will give, for each value of Δ_p , the “working point” of the laser system. This leads to the emission profile depicted in Fig. 8(b), which has the form of a closed curve well detached from the trivial zero-intensity solution (and thus it is dramatically different with respect to the

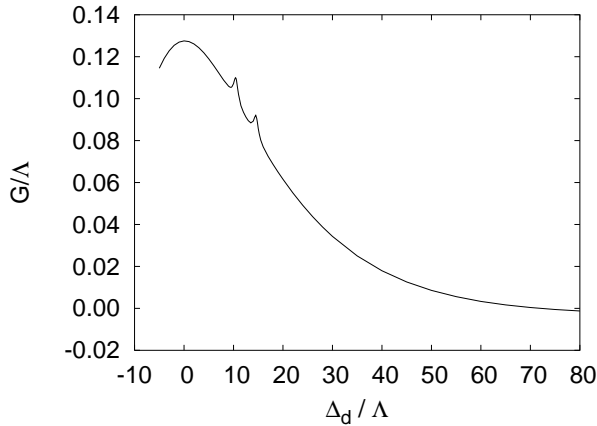


FIG. 10. Peak strength as a function of Δ_d , for the (2+2) process. $\alpha/\Lambda = 12$, $\beta/\Lambda = 15$, and other parameters as in Fig. 3.

emission profile of a standard single-photon laser, which consists of a symmetric peak connecting on both wings with the zero-intensity branch). This in particular implies that the zero-intensity solution is stable against small perturbations, and laser emission must be triggered [13].

Based on a perturbation analysis of the field amplitude, it is possible to show that the stable and unstable lasing solutions, if they exist, must be separated by points with infinite derivative. We find that the stable (unstable) solutions used to plot Fig. 8(b) correspond to the continuous (dashed) lines. Thus, there is the possibility of bistability with respect to the zero-intensity solution [there is also a narrow domain of bistability between two nonzero solutions, as shown in the inset to Fig. 8(b)]. This reasoning, however, is limited and approximate because we cannot predict the possible presence of local bifurcations that could destabilize the branches we indicate as stable, and the horizontal axis of Fig. 8(b) actually describes, for a two-photon laser, the generated *field* detuning, not the *cavity* detuning, which is usually the parameter considered in laser physics. To be able to express the emission amplitude as a function of the cavity detuning, the frequency *pushing* effect associated with the (2+2) resonance must be determined, which is given by the real part of the complex gain \tilde{G} as discussed after Eq. (6).

Investigating further details of the laser behavior, however, is difficult with the present model where the probe field is assumed to be constant. The study of different factors such as frequency pushing effects, possible overlap of two-photon lasing with other multiphoton lasing, and, most importantly, the stability and possible dynamic regimes of a two-photon laser requires a modification of our model to take fully into account the influence of the optical cavity. We will undertake such an investigation, which will be described in a subsequent paper.

To complete this study of the (2+2) gain processes we point out that the (2+2) gain peak strength approaches an asymptotic behavior that scales empirically as $[2.7 \times 10^6 + (\Delta_g/2 + \Delta_d)^4]^{-1}$ (see Fig. 10). For smaller detunings, the (2+2)-photon gain peak increases, but it splits into two features due to the ac-Stark shift and mixes with other multiphoton processes. In addition, the main absorption dip (see

Fig. 2) becomes closer to the (2+2) gain peak and thus the negative background increases. Also, there is a strong transfer of population from the initial state $|g,2,2\rangle$ to excited states (because of saturation) followed by decay to the ground states (as was also the case in Fig. 6), which makes additional single- and multiphoton coherent and incoherent (gain or absorption) processes appear, which start at different ground states. Thus, near resonance, the analysis of the probe gain absorption spectrum is more complex, and the strength of the multiphoton processes is not necessarily much larger because of the counterbalancing effect of background absorption processes.

For the sake of brevity we will not further discuss high-order processes such as the (3+2) and (3+3) ones [which are noticeable in Fig. 3(a)]. Let us mention only that, concerning the (3+3) process, its faster dependence on the drive and probe intensities and its higher saturation threshold as compared to the (2+2) process might make it more efficient at high drive and probe intensities. In the case of lasing, however, our estimations indicate that it would require a higher-intensity seeding signal, since the separation in intensity between the stable off and on solutions is larger than for the (2+2) process.

$\sum_{n=1}^3(n+n)$ -photon process

The amplification feature appearing in Figs. 2 and 3 at $\Delta_p \approx 0$ corresponds to the complex process $|g,2,2\rangle \rightarrow \alpha\beta|g,2,1\rangle \rightarrow \alpha\beta|g,2,0\rangle \rightarrow \alpha\beta|g,2,-1\rangle$, where all three intermediate steps are resonant. (Note that one further step $\rightarrow \alpha\beta|g,2,-2\rangle$ can occur, but we have ignored the contribution of states with $M = -2$, as pointed out above.) This means that the atom can go from the initial state $|g,2,2\rangle$ to any of the following final states: to state $|g,2,1\rangle$ through a (1+1)-photon Raman process, to state $|g,2,0\rangle$ through a (2+2)-photon process, or to state $|g,2,-1\rangle$ through a (3+3)-photon process. The first of these processes has already been discussed above in the context of Fig. 6 for the case of low drive and probe amplitudes, and the second of these processes is qualitatively similar to the (2+2)-photon process discussed above.

The strong overlap and interference effects among the three $\sum_n(n+n)$ processes, however, make it difficult to separate any of them, or to separate their coherent and incoherent (or step-by-step) contributions. The frequency degeneracy of the processes is lifted somewhat due to the differences in the light shifts of the final states by the intense fields. As seen in Figs. 3(a) and 3(b), when either α or β is increased, the gain peak at $\Delta_p \approx 0$ begins to split into a double-peak structure. Figure 11 shows the two peaks of this structure more separated (because of a larger drive field) for two different probe-field Rabi frequencies. It is seen that the low-frequency peak saturates more rapidly with increasing probe-beam strength, leading us to conclude that it is generated essentially by the (1+1)-photon process. In contrast, the high-frequency peak actually increases, suggesting that it arises mostly from the (2+2)-photon process. The (3+3)-photon process is not strong enough to generate a noticeable separate peak.

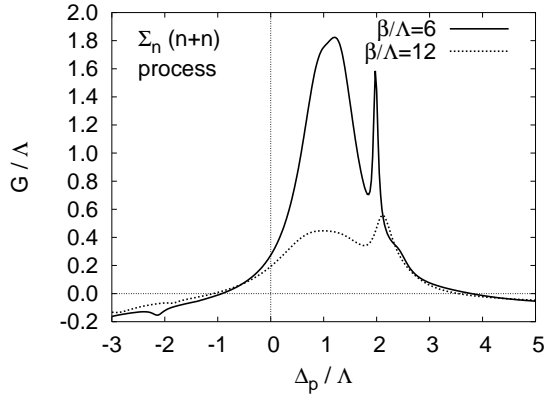


FIG. 11. Probe beam gain for the $\Sigma_n(n+n)$ -photon resonance, as a function of the probe detuning Δ_p/Λ for a drive amplitude $\alpha/\Lambda = 40$ and two values of the probe amplitude β/Λ (other parameters as in Fig. 3).

The mixed character of the $\Sigma_n(n+n)$ feature also determines the growth and saturation behavior of the gain peak strength, which is shown in Figs. 4(a) and 4(b) (for a case with $\gamma_{out}=0.3$), and obeys a law that can be seen as an overlapping among the laws governing the different $(n+n)$ processes. For instance, it is seen that the peak strength evolution differs significantly from that of the Raman (1+1)-photon resonance and shows some similarities with that of higher-order resonances. Concerning the saturation observed in Fig. 4(b), we have determined that the gain peak strength G/Λ^2 decreases with increasing probe intensity β^2/Λ as a power law with an exponent approximately given by -1.0 for large probe field (β/Λ between 25 and 80, domain only partially shown in the figure and where the peak splitting is noticeable). This value is consistent with the fact that all gain processes show asymptotically the same power dependence with probe intensity. Nevertheless, due to the negative background around $\Delta_p=0$ brought about by the proximity of the absorption resonance (Figs. 2 and 3), the absolute value of the gain peak decreases somewhat faster with the probe intensity, the power-law exponent increasing smoothly up to a value of about -1.3 for the largest values of β considered.

IV. CONCLUSIONS

In conclusion, we have investigated theoretically the multiphoton gain features arising in the interaction of a drive and a probe field of arbitrary intensities with the D_1 transition of an alkali-metal atom, taking into account most of the hyperfine sublevels. We used the theory to predict gain spectra for the situation of ^{39}K that was used in recent experiments demonstrating two-photon amplification [16] and lasing [7]. Our results are in very good agreement with the experimental findings concerning gain [16], allowing us to confirm the origin of essentially all the observed features. In addition, we are able to study the effects of interference among different quantum pathways contributing to the observed resonance, giving deeper insight into their origin. The influence of the different physical factors and parameters can easily be studied with our model, giving important information about two-

TABLE II. Translation from atomic notation to numeric notation.

$ e,2,2\rangle \rightarrow 1$	$ g,2,2\rangle \rightarrow 2$
$ e,1,1\rangle \rightarrow 3$	$ e,2,1\rangle \rightarrow 4$
$ g,2,1\rangle \rightarrow 5$	$ g,1,1\rangle \rightarrow 6$
$ e,1,0\rangle \rightarrow 7$	$ e,2,0\rangle \rightarrow 8$
$ g,2,0\rangle \rightarrow 9$	$ g,1,0\rangle \rightarrow 10$
$ e,1,-1\rangle \rightarrow 11$	$ e,2,-1\rangle \rightarrow 12$
$ g,2,-1\rangle \rightarrow 13$	$ g,1,-1\rangle \rightarrow 14$

photon lasing, including the emission spectral profile that can be expected.

Our results greatly extend the theoretical results published in [17], where a more simplified model was considered. The present model can describe, for instance, multiphoton processes of larger order, the radiative shifts of the multiphoton resonances, and the expected two-photon laser emission profile.

Future work will incorporate into our model the role played by an optical cavity, so that it will be possible to completely determine the two-photon laser emission characteristics and to study the stability and possible dynamics of such emission. This model will also allow us to determine the operating conditions for which the two-photon emission is immune to perturbations by single-photon and three-photon emission, which are possible competing processes. In this way we will be able to understand the recent experimental results on two-photon lasing [7] and to establish a basis for theoretical investigation of whether the laser produces polarization-entangled twin beams.

ACKNOWLEDGMENTS

We acknowledge financial support from the DGESIC (Spanish Government) through Project No. BFM2002-04369-C04-C03 and the Generalitat de Catalunya through Project No. 2001SGR 00223. D.J.G. and A.K. gratefully acknowledge the financial support of the U.S. National Science Foundation through Grant No. PHY-0139991.

APPENDIX

In this appendix we give the mathematical expressions for several of the equations included in Eq. (1), which describe the evolution of the most representative density-matrix elements characterizing the field-matter interaction. To simplify the expressions, we identify the atomic state using a numeric notation displayed in Table II.

The equations described below include the evolution of the population of state 2, which is the most populated state initially, and of one atomic coherence of each possible order connecting that state with other atomic states. Specifically, we consider the population $\rho_{2,2} \equiv x_{2,2}$, and the single-photon coherence $\rho_{3,2} \equiv x_{3,2} + iy_{3,2}$, the two-photon coherence $\rho_{2,5} \equiv x_{2,5} + iy_{2,5}$, the three-photon coherence $\rho_{2,7} \equiv x_{2,7} + iy_{2,7}$, the four-photon coherence $\rho_{2,10} \equiv x_{2,10} + iy_{2,10}$, the five-photon coherence $\rho_{2,11} \equiv x_{2,11} + iy_{2,11}$, the six-photon coher-

ence $\rho_{2,14} \equiv x_{2,14} + iy_{2,14}$ and the seven-photon coherence $\rho_{1,14} \equiv x_{1,14} + iy_{1,14}$. Each one of these coherence envelopes is related to the strength of the corresponding multiphoton process connecting its associated initial and final atomic states.

$$\begin{aligned} \dot{x}_{2,2} = & \lambda_2 + \gamma_{2,1}x_{1,1} + \gamma_{2,3}x_{3,3} + \gamma_{2,4}x_{4,4} + \gamma_{2,5}x_{5,5} + \gamma_{2,6}x_{6,6} \\ & - (\gamma_{5,2} + \gamma_{6,2} + \gamma_{out})x_{2,2} - 2[\chi_{1,2}\beta y_{1,2} + \alpha(\chi_{2,3}y_{3,2} \\ & + \chi_{2,4}y_{4,2})], \end{aligned} \quad (\text{A1})$$

$$\begin{aligned} \dot{x}_{3,2} = & -\Gamma_{3,2}x_{3,2} - (\Delta_d + \Delta_e + \Delta_g)y_{3,2} + \beta(\chi_{3,5}y_{2,5} + \chi_{3,6}y_{2,6} \\ & - \chi_{1,2}y_{1,3}) + \alpha\chi_{2,4}y_{4,3}, \end{aligned} \quad (\text{A2})$$

$$\begin{aligned} \dot{y}_{3,2} = & -\Gamma_{3,2}y_{3,2} + (\Delta_d + \Delta_e + \Delta_g)x_{3,2} + \chi_{2,3}\alpha(x_{2,2} - x_{3,3}) \\ & + \beta(\chi_{3,5}x_{2,5} + \chi_{3,6}x_{2,6} - \chi_{1,2}x_{1,3}) - \chi_{2,4}\alpha x_{4,3}, \end{aligned} \quad (\text{A3})$$

$$\begin{aligned} \dot{x}_{2,5} = & -\Gamma_{2,5}x_{2,5} - y_{2,5}(\Delta_p) + \alpha(\chi_{5,7}y_{2,7} + \chi_{5,8}y_{2,8} - \chi_{2,3}y_{3,5} \\ & - \chi_{2,4}y_{4,5}) - \beta(\chi_{1,2}y_{1,5} + \chi_{3,5}y_{3,2} + \chi_{4,5}y_{4,2}), \end{aligned} \quad (\text{A4})$$

$$\begin{aligned} \dot{y}_{2,5} = & -\Gamma_{2,5}y_{2,5} + x_{2,5}(\Delta_p) + \alpha(\chi_{2,3}x_{3,5} + \chi_{2,4}x_{4,5} - \chi_{5,7}x_{2,7} \\ & - \chi_{5,8}x_{2,8}) + \beta(\chi_{1,2}x_{1,5} - \chi_{3,5}x_{3,2} - \chi_{4,5}x_{4,2}), \end{aligned} \quad (\text{A5})$$

$$\begin{aligned} \dot{x}_{2,7} = & -\Gamma_{2,7}x_{2,7} + y_{2,7}(\Delta_d + \Delta_e + \Delta_g - \Delta_p) + \alpha(\chi_{5,7}y_{2,5} \\ & + \chi_{6,7}y_{2,6} - \chi_{2,4}y_{4,7} - \chi_{2,3}y_{3,7}) + \beta(\chi_{7,10}y_{2,10} - \chi_{1,2}y_{1,7} \\ & + \chi_{7,9}y_{2,9}), \end{aligned} \quad (\text{A6})$$

$$\begin{aligned} \dot{y}_{2,7} = & -\Gamma_{2,7}y_{2,7} - x_{2,7}(\Delta_d + \Delta_e + \Delta_g - \Delta_p) + \alpha(\chi_{2,3}x_{3,7} \\ & + \chi_{2,4}x_{4,7} - \chi_{5,7}x_{2,5} - \chi_{6,7}x_{2,6}) + \beta(\chi_{1,2}x_{1,7} - \chi_{7,9}x_{2,9} \\ & - \chi_{7,10}x_{2,10}), \end{aligned} \quad (\text{A7})$$

$$\begin{aligned} \dot{x}_{2,10} = & -\Gamma_{2,10}x_{2,10} + y_{2,10}[\Delta_g - 2(\Delta_p)] + \alpha(\chi_{10,11}y_{2,11} \\ & + \chi_{10,12}y_{2,12} - \chi_{2,3}y_{3,10} - \chi_{2,4}y_{4,10}) + \beta(\chi_{7,10}y_{2,7} \\ & + \chi_{8,10}y_{2,8} - \chi_{1,2}y_{10,11}), \end{aligned} \quad (\text{A8})$$

$$\begin{aligned} \dot{y}_{2,10} = & -\Gamma_{2,10}y_{2,10} - x_{2,10}[\Delta_g - 2(\Delta_p)] + \alpha(\chi_{2,3}x_{3,10} \\ & + \chi_{2,4}x_{4,10} - \chi_{10,11}x_{2,11} - \chi_{10,12}x_{2,12}) + \beta(\chi_{1,2}x_{1,10} \\ & - \chi_{7,10}x_{2,7} - \chi_{8,10}x_{2,8}), \end{aligned} \quad (\text{A9})$$

$$\begin{aligned} \dot{x}_{2,11} = & -\Gamma_{2,11}x_{2,11} + y_{2,11}[\Delta_d + \Delta_e + \Delta_g - 2(\Delta_p)] \\ & + \alpha(\chi_{10,11}y_{2,10} + \chi_{9,11}y_{2,9} - \chi_{2,4}y_{4,11} - \chi_{2,3}y_{3,11}) \\ & + \beta(\chi_{11,14}y_{2,14} + \chi_{11,13}y_{2,13} - \chi_{1,2}y_{10,11}), \end{aligned} \quad (\text{A10})$$

$$\begin{aligned} \dot{y}_{2,11} = & -\Gamma_{2,11}y_{2,11} - x_{2,11}[\Delta_d + \Delta_e + \Delta_g - 2(\Delta_p)] \\ & + \alpha(\chi_{2,3}x_{3,11} + \chi_{2,4}x_{4,11} - \chi_{10,11}x_{2,10} - \chi_{9,11}x_{2,9}) \\ & + \beta(\chi_{1,2}x_{1,11} - \chi_{11,14}x_{2,14} - \chi_{11,13}x_{2,13}), \end{aligned} \quad (\text{A11})$$

$$\begin{aligned} \dot{x}_{2,14} = & -\Gamma_{2,14}x_{2,14} + y_{2,14}[\Delta_g - 3(\Delta_p)] - \alpha(\chi_{2,3}y_{3,14} \\ & + \chi_{2,4}y_{4,14}) + \beta(\chi_{11,14}y_{2,11} + \chi_{12,14}y_{2,12} - \chi_{1,2}y_{1,14}), \end{aligned} \quad (\text{A12})$$

$$\begin{aligned} \dot{y}_{2,14} = & -\Gamma_{2,14}y_{2,14} - x_{2,14}[\Delta_g - 3(\Delta_p)] + \alpha(\chi_{2,3}x_{3,14} \\ & + \chi_{2,4}x_{4,14}) + \beta(\chi_{1,2}x_{1,14} - \chi_{11,14}x_{2,11} - \chi_{12,14}x_{2,12}), \end{aligned} \quad (\text{A13})$$

$$\begin{aligned} \dot{x}_{1,14} = & -\Gamma_{1,14}x_{1,14} - y_{1,14}[\Delta_d + 4(\Delta_p)] + \beta(\chi_{11,14}y_{1,11} \\ & + \chi_{12,14}y_{1,12} - \chi_{1,2}y_{2,14}), \end{aligned} \quad (\text{A14})$$

$$\begin{aligned} \dot{y}_{1,14} = & -\Gamma_{1,14}y_{1,14} + x_{1,14}[\Delta_d + 4(\Delta_p)] + \beta(\chi_{1,2}x_{2,14} \\ & - \chi_{11,14}x_{1,11} - \chi_{12,14}x_{1,12}). \end{aligned} \quad (\text{A15})$$

-
- [1] D. J. Gauthier, in *Progress in Optics* (Elsevier, North-Holland, 2003), Vol. 45.
- [2] D.R. Heatly, W.J. Firth, and C.N. Ironside, *Opt. Lett.* **18**, 628 (1993).
- [3] R. Vilaseca, M. Torrent, J. García-Ojalvo, M. Brambilla, and M.S. Miguel, *Phys. Rev. Lett.* **87**, 083902 (2001).
- [4] S. Swain, *Phys. Rev. A* **41**, 343 (1990).
- [5] M. D'Angelo, M. Chekhova, and Y. Shih, *Phys. Rev. Lett.* **87**, 013602 (2001).
- [6] G. Björk, L. Sánchez-Soto, and J. Söderholm, *Phys. Rev. Lett.* **86**, 4516 (2001).
- [7] O. Pfister, W.J. Brown, M.D. Stenner, and D.J. Gauthier, *Phys. Rev. Lett.* **86**, 4512 (2001).
- [8] L. Narducci, W. Eidson, P. Furcinitti, and D. Eteson, *Phys. Rev. A* **16**, 1665 (1977).
- [9] C.Z. Ning and H. Haken, *Z. Phys. B: Condens. Matter* **77**, 157 (1989).
- [10] G. de Valcárcel, E. Roldán, J. Urchueguía, and R. Vilaseca, *Phys. Rev. A* **52**, 4059 (1995).
- [11] J. Zakrezewski and M. Lewenstein, *Phys. Rev. A* **45**, 2057 (1992).
- [12] B. Nikolaus, D. Zhang, and P. Toschek, *Phys. Rev. Lett.* **47**, 171 (1981).
- [13] D.J. Gauthier, Q. Wu, S.E. Morin, and T.W. Mossberg, *Phys. Rev. Lett.* **68**, 464 (1992).
- [14] D. Jackson and J. Wynne, *Appl. Phys. B: Photophys. Laser Chem.* **28**, 238 (1982).
- [15] J. Sparbier, K.-J. Boller, and P. Toschek, *Phys. Rev. A* **62**, 227

- (1996).
- [16] O. Pfister, W.J. Brown, M.D. Stenner, and D.J. Gauthier, *Phys. Rev. A* **60**, R4249 (1999).
- [17] J.J. Fernández-Soler, J.L. Font, R. Vilaseca, D.J. Gauthier, A. Kul'minskii, and O. Pfister, *Phys. Rev. A* **65**, 031803 (2002).
- [18] C. Weiss and R. Vilaseca, *Dynamics of Lasers* (VCH, Weinheim, 1991).
- [19] P. Mandel, *Theoretical Problems in Cavity Nonlinear Optics* (Cambridge University Press, Cambridge, England, 1997).
- [20] Y. Khanin, *Principles of Laser Dynamics* (North-Holland, Amsterdam, 1995).
- [21] J. Dodd, *Atoms and Light Interactions* (Plenum Press, New York, 1991).
- [22] L. Allen and C.R. Stroud, *Phys. Rep.* **91**, 1 (1982).
- [23] H.M. Concannon, W.J. Brown, J.R. Gardner, and D.J. Gauthier, *Phys. Rev. A* **56**, 1519 (1997).